Sensorless Position Control of Synchronous Reluctance Motor with Real Time Path Generation

Federico Centi, Andrea Credo, Guiseppe Fabri, Rama Salloum, Marco Tursini

Sensorless Position Control of Synchronous Reluctance Motor with Real Time Path Generation

F. Centi, A. Credo, G. Fabri, R. Salloum, M. Tursini
Department of Industrial and Information Engineering and Economy
University of L'Aquila,
Piazzale E. Pontieri - Monteluco di Roio, 67100 L'Aquila
L'Aquila, Italy
E-Mail: federico.centi@graduate.univaq.it, andrea.credo@univaq.it, giuseppe.fabri@univaq.it, rama.salloum@univaq.it, marco.tursini@univaq.it

Acknowledgements

In This work has been funded by the European Union - NextGenerationEU under the Italian Ministry of University and Research (MUR) National Innovation Ecosystem grant ECS00000041 - VITALITY - CUP E13C220010 60006

Keywords

«Electrical drive», «Motion control», «Position measurement»,, «Sensorless control», «Synchronous Reluctance Machine (SynRM)».

Abstract

This paper presents a sensorless position control for synchronous reluctance motors with real-time path generation. Sensorless control employs high-frequency flux injection with digital demodulation by sampling. The path generation is embedded in the drive microcontroller making available the use of fast feedforward actions both in the control loops and in the sensorless engine. The experimental results show the feasibility of the approach although the intrinsic position estimation error of the high-frequency injection limits the speed range.

Introduction

Tracking position control of electric motors is crucial to achieve precise and reliable performance in various applications. The generation of a motion profile (position, velocity, and accelerations) compatible with the mission requirements and the limits of the actuator is the so-called "path generation problem". In autonomous navigation systems (such as robots, drones, or autonomous vehicles), the path is subject to continuous updating based on the current position, obstacles, and goals, ensuring the entity can safely and efficiently reach its destination still in the presence of changes in the environment. Hence, the path generation problem must be processed in real- time.

Advanced regulators, including PID controllers [1], model predictive control [2], and sliding mode control [3], are widely implemented to ensure accurate position regulation.

However, the position sensor can potentially increase the overall volume of the machine, decrease the system reliability and dependability, and lead to an increase in manufacturing costs.

Sensorless position control techniques have been used recently to estimate the rotor's position and avoid these weak points. These techniques estimate the rotor position by analyzing electrical signals specific to the operation or specially injected, depending on the motor type [4].

In synchronous motors featuring magnetic anisotropy in the rotor, the position of this last can be estimated by injecting high-frequency signals into the stator windings [5][6], and the estimation is stable at a standstill, allowing its application in position control.

For Synchronous Reluctance (SynRel) motors, specifically, high-frequency techniques should address the motor's inherent nonlinearity to improve the accuracy of estimation and enhance the overall drive efficiency and robustness, and this is still a challenging research topic [7].

Indeed, the lack of rare-earth materials, low cost, comparable constant-power speed range, and efficiency (with respect to permanent magnet motors) have made SynRel an interesting choice in the increasing market of electric traction [8].

This paper presents the sensorless position control of a SynRel motor drive based on high-frequency signal injection and real-time path generation.

Updating the proposal in [9], triangular-waved flux injection is proposed instead of sinusoidal voltage injection, while demodulation by sampling is applied on the stator currents to speed up the process.

Following the proposals in [10][11] the problem of path generation is analytically stated having the motion constraints as inputs and the tracking acceleration, speed and position as outputs. This paper presents the solution for the jerk-free profile in discretized form, that is used for the real-time implementation in the drive controller.

The paper is organized as follows: the 2nd section introduces the sensorless position control, the 3rd section outlines the flux-injection method, the 4th section presents the tracking motion profiles, and the 5th section shows the experimental results. These last are obtained from a 75kW SynRel motor drive designed for e-traction.

Sensorless position control

The control scheme in the case of signal injection sensorless position control with real-time path generation is shown in Fig. 1.

The position error is calculated from the difference between the target and the estimated positions of the motor shaft. Multivariable PI controllers are used to regulate the d- and q-axis currents according to the MTPA (Maximum Torque per Ampere) optimization, while standard PI and simple P regulators are used for the speed and position loops, respectively. Space Vector PWM is used for inverter modulation.

The Band-Pass Filter (BPF) extracts the high-frequency current signals to obtain the necessary information for position estimation and speed in a Quadrature Phase-Locked Loop (QPLL). The path generator provides the run-time signals for the position reference and the speed control feed-forward, according to the target motion requirements. In this paper, the use of the feed-forward signals of acceleration and speed is proposed to enhance the dynamics of the QPLL scheme in the sensorless loop.

Signal injection

The signal injection technique employed is briefly recalled in the following.

Supposing to inject high-frequency flux in the estimated $\hat{d}$-$\hat{q}$ rotor frame, the corresponding current components are (see Fig. 2 and the Appendix 1 for the symbol's meaning):

$$\begin{bmatrix} \delta I_{i\hat{d}} \\ \delta I_{i\hat{q}} \end{bmatrix} = \underset{dq\to\hat{d}\hat{q}}{\boldsymbol{T}(\Delta\theta)} \boldsymbol{L}^{-1} \underset{dq\to\hat{d}\hat{q}}{\boldsymbol{T}(\Delta\theta)^{-1}} \begin{bmatrix} \delta\Psi_{i\hat{d}} \\ \delta\Psi_{i\hat{q}} \end{bmatrix} \tag{1}$$

where the differential uncoupled inductance model around the flux working point P is considered:

$$\boldsymbol{L} = \begin{bmatrix} l_{d(P)} & 0 \\ 0 & l_{q(P)} \end{bmatrix}$$

From this assumption and by supposing to inject triangular-shaped flux on the $\hat{q}$-axis only, that is:

$$\begin{aligned} &\delta\Psi_{i\hat{d}} = 0 \\ &\delta\Psi_{i\hat{q}} = 4\hat{\Psi}_i \left| \left[\left(t - \frac{T_i}{4} \right) mod(T_i) \right] - \frac{T_i}{2} \right| - \hat{\Psi}_i \end{aligned} \tag{2}$$

we obtain:

$$\begin{bmatrix} \delta I_{i\hat{d}} \\ \delta I_{i\hat{q}} \end{bmatrix} = \frac{\delta\Psi_{i\hat{q}}}{l_d l_q} \begin{bmatrix} -l_\Delta sin2\Delta\theta \\ l_\Sigma - l_\Delta cos2\Delta\theta \end{bmatrix} \tag{3}$$

The corresponding current components in the stationary α-β reference are:

$$\begin{bmatrix} \delta I_{i\alpha} \\ \delta I_{i\beta} \end{bmatrix} = \underset{\hat{d}\hat{q}\to\alpha\beta}{\left[T(\hat{\theta}_r) \right]} \cdot \begin{bmatrix} \delta I_{i\hat{d}} \\ \delta I_{i\hat{q}} \end{bmatrix} \tag{4}$$

Substituting (1) in (4) and accounting for the axis transformation one achieves:

$$\begin{bmatrix} \delta I_{i\alpha} \\ \delta I_{i\beta} \end{bmatrix} = \frac{\delta\Psi_{i\hat{q}}}{l_d l_q} \boldsymbol{\Lambda} \tag{5}$$

with:

$$\boldsymbol{\Lambda} = \begin{bmatrix} -l_\Delta sin(2\Delta\theta) cos\hat{\theta}_r - (l_\Sigma - l_\Delta cos(2\Delta\theta)) sin\hat{\theta}_r \\ -l_\Delta sin(2\Delta\theta) sin\hat{\theta}_r + (l_\Sigma - l_\Delta cos(2\Delta\theta)) cos\hat{\theta}_r \end{bmatrix}$$

According to the principle of demodulation by sampling, the high-frequency currents (5) can be sampled at the peaks of the triangular-waved flux (2) to achieve the envelopes $\Delta I_{i\alpha}$ and $\Delta I_{i\beta}$.

$$\begin{bmatrix} \Delta I_{i\alpha} \\ \Delta I_{i\beta} \end{bmatrix} = \frac{\hat{\Psi}_i}{l_d l_q} \boldsymbol{\Lambda} \tag{6}$$

If one accounts for an engine able to maintain the difference $\Delta\vartheta = 0$ at run-time, such an high dynamics PLL, the demodulated components give:

$$\begin{bmatrix} \Delta I_{i\alpha} \\ \Delta I_{i\beta} \end{bmatrix} \approx 2 \frac{\hat{\Psi}_i}{l_q} \begin{bmatrix} -sin(\theta_r) \\ cos(\theta_r) \end{bmatrix} \tag{7}$$

Thereafter, providing the respective $-sin(\vartheta)$ and $cos(\vartheta)$ waveforms, a quadrature PLL algorithm can be used to compute the inherent rotor position and speed.

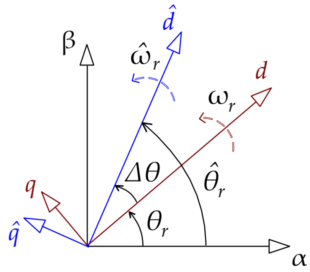

Fig. 1: Actual (d-q) vs. estimated ($\hat{d}$-$\hat{q}$) rotor reference frames and stator reference (α-β)

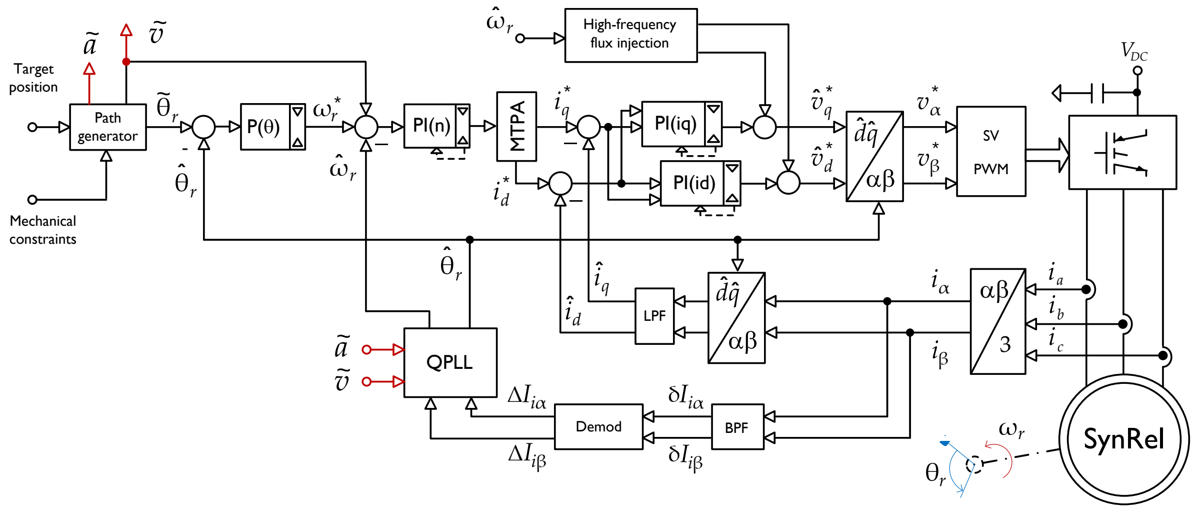

Fig. 2: Signal injection sensorless position control with real-time path generation

Finally, the flux injection (2) is provided by the voltages:

$$\delta V_{i\hat{d}} = 0$$
$$\delta V_{i\hat{q}} = \hat{V}_i \cdot sign\{cos(\omega_i t)\} \quad (8)$$

with $\hat{V}_i = \frac{2}{\pi}\omega_i \hat{\Psi}_i$ and $\omega_i = 2\pi/T_i$. These relations are computed by assuming near-to-zero speed operation, as detailed in Appendix 2: thereafter, an estimation error is predictable at increasing speed whose evaluation is among the goals of the paper.

Fig. 3 shows an operating case of the signal injection technique (experimental). The high-frequency signal is injected at 625 Hz and the fundamental operation of the case is about 12 Hz. In discrete-time digital implementation the injection frequency is selected as an even integer submultiple of the PWM/control frequency (10 kHz).

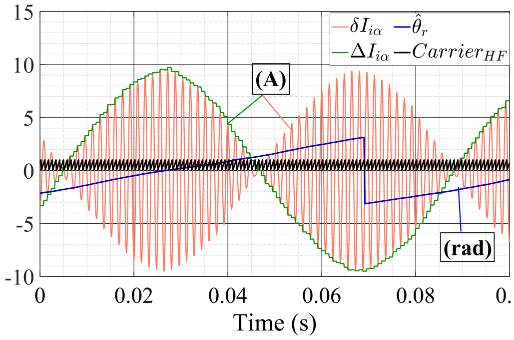

Fig. 3: Demodulation of the high-frequency currents: high-frequency carrier (black), estimated rotor position (blue), high-frequency current α (red), demodulated α current (green)

The demodulation is obtained by sampling the high frequency currents so to capture the signed maximum value in each half-period.

Details on this implementation (and other results presented in this section) are given in Appendix 2.

Path generation

Path generation is a crucial aspect of position control for motion control drives which can be schematically represented as in Fig. 4.

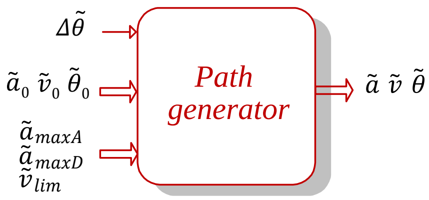

Fig. 4: The path generation problem

It involves calculating the optimal trajectory of acceleration ($\tilde{a}$), speed ($\tilde{v}$), and tracking position ($\tilde{\theta}$) that the motor should follow to achieve precise positioning from a given initial state ($\tilde{a}_0, \tilde{v}_0, \theta_0$) and constraints ($\tilde{a}_{maxA}, \tilde{a}_{maxD}, \tilde{v}_{lim}$). Specific and wide literature is available in this area, deepening aspect outside the scope of the present paper. As references, a comprehensive presentation of the motion laws for actuation systems based on electric drives can be found in [12], while a method to find the movement parameters leading to maximizing efficiency and minimizing energy consumption is presented in [13].

The jerk-free profile of acceleration has been used in this paper, Fig. 5 (experimental). This profile allows for smooth acceleration and deceleration beneficial for applications where abrupt changes in velocity or position are undesirable and, generally, in reducing mechanical stress and wear on the system components.

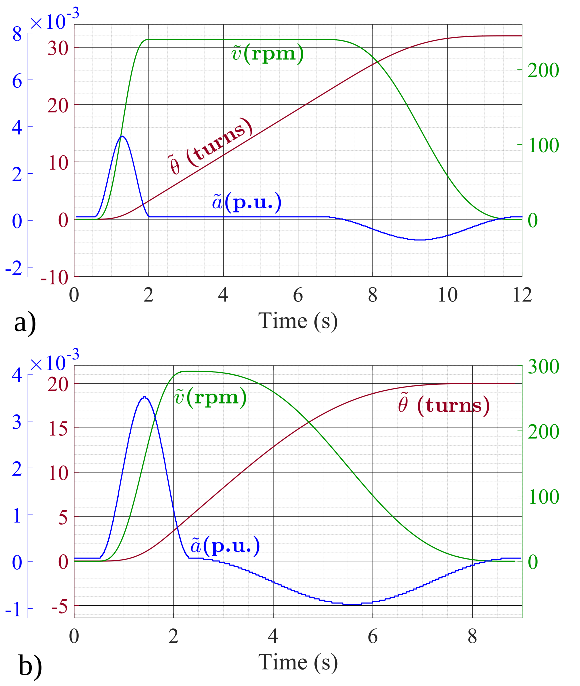

Fig. 5: Jerk-free path profiles: with a) and without b) constant speed period.

Moreover, in the high-frequency sensorless method, the gradual acceleration and deceleration allow for reducing the transient estimation error intrinsic to such a technique.

Below the equations of the jerk-free profile are resumed.

Starting from what is presented in [10], the time formulas of the acceleration, speed, and position are expressed as follows (the per-unit form is presented, whose coefficients k_{ipV} and k_{ipT} are detailed in Appendix 1).

Acceleration period

$$\tilde{a}_A(t) = A_A\left[\frac{1}{2} - \frac{1}{2}cos\left(2\pi\frac{t}{t_{sA}}\right)\right]$$

$$\tilde{v}_A(t) = 2V_A\left[\frac{t}{t_{sA}} - \frac{1}{2\pi}sin\left(2\pi\frac{t}{t_{sA}}\right)\right] + \tilde{v}_0 \tag{9}$$

$$\tilde{\theta}_A(t) = 2h_A\left[\frac{t^2}{2t_{sA}^2} + \frac{1}{8\pi^2}\left(cos\left(2\pi\frac{t}{t_{sA}}\right) - 1\right)\right] + h_{v0}\frac{t}{t_{sA}} + \tilde{\theta}_{0A}$$

where $\Delta\tilde{v} = \tilde{v}_{max0} - \tilde{v}_0$,

$$|\tilde{v}_{max0}| = \sqrt{\frac{\Delta\tilde{\theta}\frac{k_{ipV}}{k_{ipT}}|\tilde{a}_{maxA}||\tilde{a}_{maxD}| + sign(\Delta\tilde{v})\cdot\tilde{v}_0^2|\tilde{a}_{maxD}|}{sign(\Delta\tilde{v})\cdot|\tilde{a}_{maxD}| + sign(\Delta\tilde{v}')\cdot|\tilde{a}_{maxA}|}} \tag{10}$$

is the maximum speed reached at time

$$t_{sA} = 2\frac{|\tilde{v}_{max0} - \tilde{v}_0|}{k_{ipV}|\tilde{a}_{maxA}|}$$

and

$$h_A = k_{ipT}(\tilde{v}_{max0} - \tilde{v}_0)\,\frac{t_{sA}}{2}$$

$$h_{v0} = k_{ipT}t_{sA}\tilde{v}_0$$

are the (signed) movement components in time t_{sA}. The case of $\tilde{v}_0$ <> 0 stands for a path change during its execution; it is not considered in the following.

Deceleration period

$$\tilde{a}_D(t") = A_D\left[\frac{1}{2} - \frac{1}{2}cos\left(2\pi\frac{t"}{t_{sD}}\right)\right]$$

$$\tilde{v}_D(t") = 2V_D\left[\frac{t"}{t_{sD}} - \frac{1}{2\pi}sin\left(2\pi\frac{t"}{t_{sD}}\right)\right] + \tilde{v}_{max0} \tag{11}$$

$$\tilde{\theta}_D(t") = -2h_D\left[\frac{t"^2}{2t_{sD}^2} + \frac{1}{8\pi^2}\left(cos\left(2\pi\frac{t"}{t_{sD}}\right) - 1\right) - \frac{t"}{t_{sD}}\right] + \tilde{\theta}_{0D}$$

where $\Delta\tilde{v}' = 0 - \tilde{v}_{max0}$, the zero speed is reached at time

$$t_{sD} = 2\frac{|-\tilde{v}_{max0}|}{k_{ipV}|\tilde{a}_{maxD}|}$$

and

$$h_D = k_{ipT}\tilde{v}_{max0}\frac{t_{sD}}{2}$$

is the (signed) movement in time t_{sD}.

Constant speed period

If the max speed computed from (10) exceeds the limit (constraint) value $\tilde{v}_{lim}$ the path will have to include a constant speed period with relations:

$$\tilde{a}_C(t') = 0$$

$$\tilde{v}_C(t') = \tilde{v}_{lim} \tag{12}$$

$$\tilde{\theta}_C(t') = h_C\frac{t'}{t_{sC}} + \tilde{\theta}_{0C}$$

where:

$$h_c = \Delta\tilde{\theta} - (h_A + h_{v0} + h_D)$$

is the (signed) movement during the constant speed period of length $t_{sC} = h_c/(k_{ipT}|\tilde{v}_{lim}|)$, and $\tilde{v}_{max0} = \tilde{v}_{lim}$ will have to be used in calculations for the acceleration and deceleration periods.

Discrete time form

To achieve the discretized form needed for real time implementation we introduce in the different period $x = A, C, D$ the time fraction $\delta_{Px}(\tau) = \tau/t_{sx}$ with $0 \leq \delta_{Px} \leq 1$ and by discretizing with sampling period $\Delta\tau = \tau_{k-1} - \tau_k$ we can replace the terms τ/t_{sx} in relations (8), (10), and (12) by:

$$\delta_{Px}(\tau_k) = \delta_{Px}(\tau_{k-1}) + \frac{\Delta\tau}{t_{sx}}$$

for the sake of iterative computation.

Experimental results

The experimental system used in this paper is shown in Fig. 6. It includes the 75 kW, six-pole SynRel motor with frame-integrated three-phase 750V Silicon Carbide inverter and control unit based on a TI Delfino F28379S 200 MHz microcontroller.

Fig. 6: Experimental setup and drive

The inverter PWM period is 100 µs, equals to the sampling time of the control algorithm. Real-time monitoring is achieved by fast RS232 link to the host PC.

A resolver sensor is used to measure the rotor's actual position and speed, featuring 16384 pulses for rotor turn.

Due to the limitations of the available drive system, the experimental tests were conducted at no-load and reduced inverter DC voltage of 170 V.

Fig. 7 shows the experimental behaviours obtained by imposing the jerk-free path profiles in Fig. 5. The position trace refers to the estimated feedback used to close the control loop, while the speed and acceleration signals are computed from the resolver sensor. The shapes of the actual variables reflect quite well the requested path profiles, discrepancies are due to the control action, such as the speed overshoot and the oscillation at the final standstill.

The following figures detail the sensorless performance for the path with constant speed a).

Fig. 8 represents the estimated angle of the rotor and the angle measured by the resolver during the acceleration period. The good alignment between the curves shows that the control system tracks the reference angle well in transient operation.

Fig. 9 illustrates the relationship between the speed and the angle error (the difference between the measured and the estimated one, expressed in electrical radians). It's noticed that at the beginning when the speed is almost zero, the angle error is also about zero. During the acceleration, between 1-2 seconds, there is a rapid and significant change in the speed, and the angle error arises up to about 20 degrees at steady state from 2 until 4 seconds. Between 4 to 6 seconds, there is another transition period, due to deceleration; after it, the system goes back to the initial state.

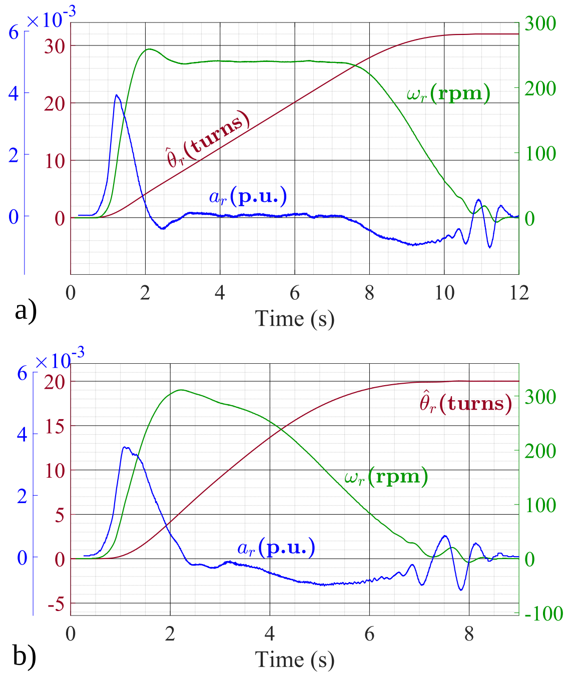

Fig. 7: Jerk-free path actual variables: with a) and without b) constant speed period

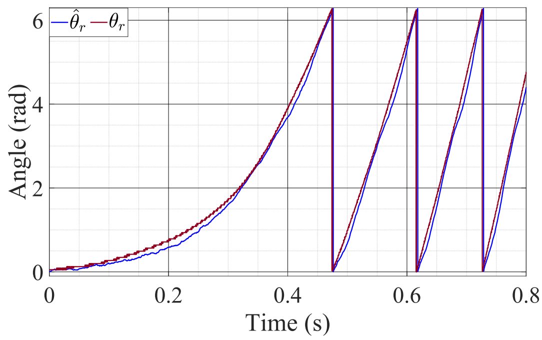

Fig. 8: Estimated and measured rotor angle

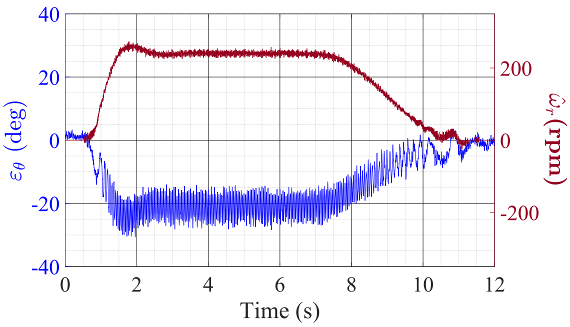

Fig. 9: Speed and angle error

Fig. 10 shows the estimated speed vs. the measured one by the resolver sensor. The resolver speed shows a more stable and less noisy signal compared to the estimated speed that has oscillation throughout the entire period.

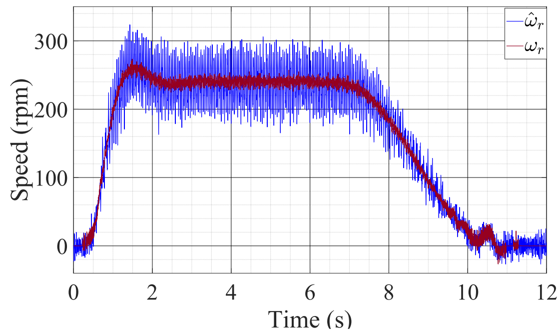

Fig. 10: Measured and estimated speed

Conclusions

In this paper, a sensorless position control for synchronous reluctance motors based on high-frequency signal injection has been presented. Real-time path profiles have provided signal references for position control. The results show that the control system accurately tracks the commanded paths despite the presence of a speed-dependent error in the estimated angle. Further work will investigate some solutions to reduce this speed-dependent error which must be contained within acceptable limits to ensure safe operation and avoid performance loss.

References

[1]. P. Rocco, "Stability of PID control for industrial robot arms," in IEEE Transactions on Robotics and Automation, vol. 12, no. 4, pp. 606-614, Aug. 1996

[2]. M. A. Stephens, C. Manzie and M. C. Good, "Model Predictive Control for Reference Tracking on an Industrial Machine Tool Servo Drive," in IEEE Transactions on Industrial Informatics, vol. 9, no. 2, pp. 808-816, May 2013

[3]. W. Shen, L. Shao, D. Liu, J. Wang and C. Ge, "Event-Triggered FCS-MPC With Sliding Mode Observer for Permanent Magnet Synchronous Motor Servo Motion Systems," in IEEE Transactions on Automation Science and Engineering

[4]. Ortombina L., Pasqualotto D., Tinazzi F., and Zigliotto M.: Comprehensive Analysis and Design of a Pulsating Signal Injection-Based Position Observer for Sensorless Synchronous Motor Drives, IEEE Journal of Emerging and Selected Topics in Power Electronics, Vol. 10, no 2, April 2022

[5]. Corley M J. and Lorenz R D.: Rotor Position and Velocity Estimation for a Salient-Pole Permanent Magnet Synchronous Machine at Standstill and High Speeds, IEEE Trans. on Industry Applications, Vol. 34, no 4, July/August 1998

[6]. Yoon Y. D., Sul S. K., Morimoto S., and Ide K.: High-Bandwidth Sensorless Algorithm for AC Machines Based on Square-Wave-Type Voltage Injection, IEEE Trans. on Industry Applications, Vol. 47, no. 3, pp. 1361-1370, May-June 2011

[7]. Manzolini V. and Bolognani S.: On the Rotor Position Self-Sensing Capability of Reluctance and IPM Synchronous Motors, IEEE Trans. on Industry Applications, Vol. 56, no. 4, pp. 3755-3766, July-Aug. 2020

[8]. Credo A., Villani M., Fabri G., and Popescu M.: Adoption of the Synchronous Reluctance Motor in Electric Vehicles: A Focus on the Flux Weakening Capability, IEEE Trans. on Transportation Electrification, Vol. 9, no. 1, pp. 805-818, March 2023

[9]. Tursini M., Villani M., Fabri G., Paolini S., Credo A., and Fioravanti A.: Sensorless control of a synchronous reluctance motor by finite elements model results, 2017 IEEE Int. Symp. on Sensorless Control for Electrical Drives (SLED), pp. 19-24, Catania, Italy, 2017

[10]. Parasiliti F., Petrella R., and Tursini M.: DSP Based AC Drive Controller with Real-Time Complex Path Generation for Intelligent Motion Applications, IEEE Industry Applications Conference, Thirty-Fourth IAS Annual Meeting 1999

[11]. Bolognani S., Petrella R., Stefanutti F., and Stocco P.: Optimisation of Real-Time Complex Path Generation in Constrained Intelligent Motion Applications Based on IPM Motor Drives, International (EPE-PEMC) Power Electronics and Motion Control Conference, 2008

[12]. Biagiotti L. and Melchiorri C.: Trajectory Planning for Automatic Machines and Robots, Springer, 2009

[13]. Akbari A., Mozaffari S., Singh R., Ahmadi M., and Alirezaee S.: Movement Optimization of Robotic Arms for Energy and Time Reduction using Evolutionary Algorithms, International Symposium on Signals, Circuits and Systems (ISSCS) 2023

Appendix 1 – List of symbols

$\theta_r, \hat{\theta}_r$	Actual and estimated position
$\omega_r, \widehat{\omega}_r$	Actual and estimated speed
l_d, l_q	d, q axis inductances
l_Δ	$(l_q - l_d)/2$
l_Σ	$(l_q + l_d)/2$
$\underset{xy\rightarrow wz}{T(\delta)}$	Transformation matrix between two-phase references with phase angle δ
$\widehat{\Psi}_i, V_i$	Flux and voltage amplitudes of signal injection
T_i, ω_i	Injection period (s) and pulsation (rad/s)
$\tilde{a}, \tilde{v}, \tilde{\theta}$	Per unit acceleration, speed, and path profiles
Θ_B	Base angle (rad) = 4 π
A_B	Base acceleration (rad/s^2)
Ω_B	Base rotating speed (rad/s)
Θ_B	Base angle (rad)
k_{ipV}	A_B/Ω_B
k_{ipT}	Ω_B/Θ_B
A_A	$sign(\Delta\tilde{v})\lvert\tilde{a}_{maxA}\rvert$
V_A	$\Delta\tilde{v}/2$
A_D	$sign(\Delta\tilde{v}')\ \lvert\tilde{a}_{maxD}\rvert$
V_D	$\Delta\tilde{v}'/2$

Appendix 2 –High-frequency injection insight

Injected voltages

Equations (8) are computed by the voltage balances in the estimated $\hat{d}$-$\hat{q}$ axes assuming that resistive voltage drops are negligible (with respect to the reactive ones at the injection frequency) and by assuming near-to-zero speed operation, that is:

$$\delta V_{i\hat{d}} \cong \frac{d\delta\Psi_{i\hat{d}}}{dt}$$
$$\delta V_{i\hat{q}} = \frac{d\delta\Psi_{i\hat{q}}}{dt}$$

Sampling & Demodulation

For the implementation of the high-frequency injection algorithm a synchronizing carrier is considered as:

$$t_{HF} = \left(t + \frac{T_i}{4}\right) mod(T_i)$$

so that the injected $\hat{q}$-axis voltage (8) is:

$$\delta V_{i\hat{q}} = \hat{V}_i \cdot sign\left\{cos\left(\omega_i\left(t_{HF} - \frac{T_i}{4}\right)\right)\right\}$$

and the sampling instants of the high frequency currents for demodulation are given by $t_k^+ = \frac{T_i}{4} + kT_i$ and $t_k^- = \frac{3T_i}{4} + kT_i$ $(k = 0,1,2 \ldots)$ respectively for the positive and negative current peaks. Fig. 11 resumes the main signals behaviors.

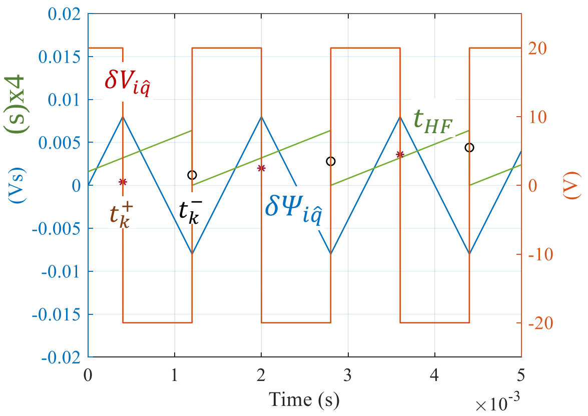

Fig. 11: Synchronizing overview of the high-frequency signals.

QPLL and observer

The scheme of the QPLL used in the sensorless algorithm is shown in Fig. 12. From equations (7) the input error of the speed and position observer is given by:

$$\varepsilon = sin(\theta_r - \hat{\theta}_r) \cong \theta_r - \hat{\theta}_r$$

by assuming small values of the position estimation error.

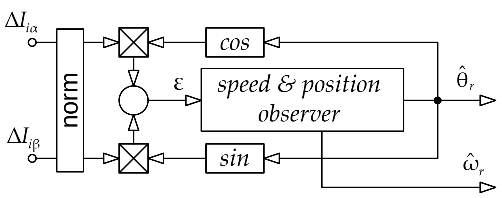

Fig. 12: QPLL scheme.

The structure of the speed and position error considered in this paper is shown in Fig. 13. It is a modified version of the PID-form observer adopted in [6] which takes advantage (as feedforward signals) of both the speed and acceleration profiles computed in run-time by the path generator, in order to enhance the dynamic response of the observer.

Fig. 14 shows the comparison between the PID-form and the standard PI-form of the observers, showing the dynamic advantage given by the first-one (simulation). The two forms are designed having the same band-pass of 250 Hz used in the experiments.

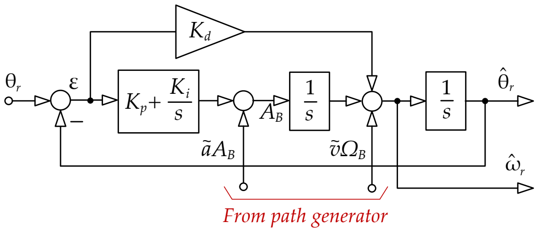

Fig. 13: Speed and position observer.

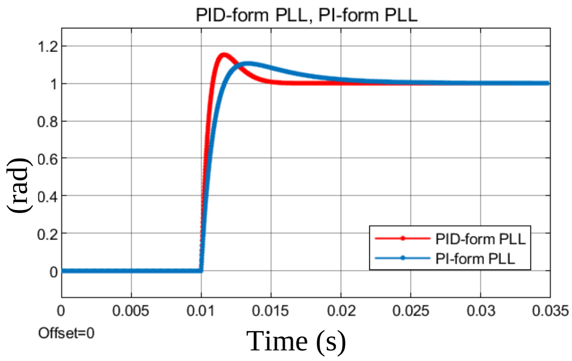

Fig. 14: Position step-response of the observer.